J. Fluid Mech. (1986), *vol.* 170, *pp.* 435–459
Printed in Great Britain

One-dimensional models for topographic Rossby waves in elongated basins on the *f*-plane

By THOMAS STOCKER AND KOLUMBAN HUTTER
Laboratory of Hydraulics, Hydrology and Glaciology, 8092-ETH Zurich, Switzerland

(Received 3 July 1985 and in revised form 25 February 1986)

Topographic Rossby waves in elongated basins on the *f*-plane are studied by transforming the linear boundary-value problem for the mass transport stream function into a class of two-point boundary-value problems of which the independent spatial variable is the (curved) basin axis. The procedure for deriving the substitute problems is the *Method of Weighted Residuals*. What emerges is a vector differential equation and associated boundary conditions, its dimension indicating the order of the approximate model. It is shown that each substitute problem in the class entails the qualitative features typical of topographic waves, and increasing the order of the model corresponds to higher-order approximations. Equations are explicitly presented for cross-sectional distributions of the lake topography which has a power-law representation and permits the analysis of weak and strong topographies.

Straight channels in which the depth profile does not change with position along the axis are studied in detail. The dispersion relation is discussed and dispersion curves are shown for the three lowest-order models. Convergence properties are thereby uncovered and phase speed and group velocity properties are found as they depend on wavenumber and topography. Further, for the lowest two modes, cross-channel stream-function distributions are presented. Apart from further convergence properties these distributions show that for U-shaped channels wave activity is nearer to the shore than for V-shaped channels, important information in the design of mooring systems.

An analysis of topographic Rossby wave reflection follows, which emphasizes the importance of the depth profile in the reflecting zone. Based on these results some lake solutions are presented.

1. Introduction

Recent years have witnessed an increased impetus in topographic wave studies in lakes. These studies arose from detailed measurements of lake currents and temperature and long periodic features discerned from them. Our own observations of thermocline oscillations in the Swiss Lakes of Lugano and Zurich show long periodic components (74 h and 100 h periods) that were believed to be interpretable as topographic wave motions (Hutter, Salvade & Schwab 1983). This is a surprise for such small-scale lakes but the observed periods could not be explained by an internal seiche mode (first-class waves) as the periods lie significantly above those of the internal seiches. A simple elliptical model was constructed (Mysak *et al.* 1985) that permitted interpretation of the observations in a qualitative sense. This model was 'tuned' to approximate the Lake Lugano geometry and bathymetry. Spectral distributions, coherences and phase differences of temperature–time series for Lake Lugano observations at the 74 h period were shown to be essentially compatible with

the topographic wave results of the elliptic model (Mysak *et al.* 1985). A similarly convincing proof was established for the Lake Zurich observations of internal oscillations with a period of approximately 100 h (K. Hutter, unpublished work).

On the other hand, recent finite-element calculations (Trösch 1984) and the required basin shape of the Mysak model indicate that topographic wave motion in these lakes may be more complex than described by the several models used so far.

Second-class motions in enclosed basins were analysed by Lamb (1932) (circular basin with parabolic bottom), Ball (1965) (elliptical basin with parabolic bottom), Saylor, Huang & Reid (1980) (fundamental-mode results for a circular basin with a radial profile described by an arbitrary power law) and Mysak *et al.* (1985) (elliptical basins whose depth contours follow confocal ellipses). Because the topographic wave operator is non-separable in general the set of analytic solutions is scarce and approximate solution techniques must be used. Such methods were first applied when Chrystal (1904, 1905) and Defant (1918) presented a set of differential equations for gravity waves in long channel-like fluid basins. The gist of their analysis was to ignore locally the fluid motion transverse to the basin axis and the result was a set of equations involving only one single independent spatial variable, the arc length along the axis. It is known that extending this so-called 'Defant model' to include the effects of the rotation of the Earth in any systematic fashion is notoriously difficult (Raggio & Hutter 1982). Because second-class motions are rotation induced, conceptual difficulties with such a model are akin to those encountered in first-class motions on a rotating basin but, given the previous experience, are easily overcome.

The basic idea is to express the transverse distribution of the mass transport field in a local curvilinear coordinate system in terms of a preselected function set and to eliminate this dependence by a 'smearing operation'. By this process, the original (spatially two-dimensional) boundary-value problem is replaced by another formulation in a domain of reduced dimension. Here, the reduced problem is a two-point boundary-value problem to be solved along the lake axis and subject to boundary conditions at the long ends of the basin. The rationale we use for the 'smearing operation' and for the deduction of the model equations is the *Method of Weighted Residuals* (MWR), which is explained in detail by Raggio & Hutter (1982). In §2 we list the governing equations and §3 contains the derivation of the approximate models using the MWR. Sections 4 and 5 present the first applications to channels and simple lakes respectively.

2. Governing equations

The conservation laws of mass and angular momentum of a homogeneous fluid in a rotating basin under no external forces can be expressed by stating that the potential vorticity Π of each fluid particle be conserved (Pedlosky 1979). If we let the vertical component of the relative vorticity be ζ, then the absolute vorticity is $\zeta+f$ and the potential vorticity is $(\zeta+f)/\overline{H}$ where the Coriolis parameter is f and the total depth of the liquid $\overline{H}$. In short,

$$\frac{\mathrm{d}\Pi}{\mathrm{d}t} = \frac{\mathrm{d}}{\mathrm{d}t}\left(\frac{\zeta+f}{\overline{H}}\right) = 0. \tag{2.1}$$

For this to hold, processes need to be adiabatic and barotropic.

In an approximate use of (2.1) small surface elevations are ignored and $\overline{H}$ is replaced by H, the equilibrium depth of the liquid. In this rigid-lid assumption the mass balance equation suggests a mass transport stream function ψ in terms of which

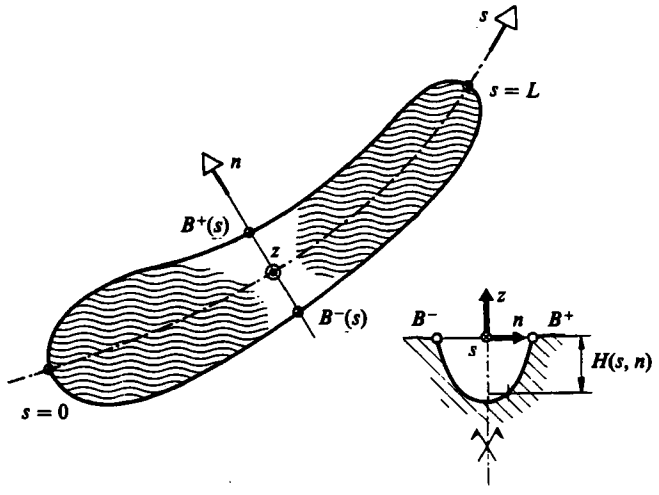

FIGURE 1. Elongated lake and transverse section in a natural (s, n, z)-coordinate system. The thalweg axis ($n = 0$) may be a centre of symmetry (not necessarily) and have curvature $K(s)$.

the depth-averaged velocity field $\boldsymbol{u}$ is given by

$$\boldsymbol{u} = \frac{1}{H}(\hat{\boldsymbol{z}} \times \nabla\psi), \tag{2.2}$$

where ∇ is the horizontal gradient operator and $\hat{\boldsymbol{z}}$ the vertical unit vector. Substituting (2.2) into (2.1), linearizing and extracting a harmonic time dependence $e^{-i\omega t}$ yields the boundary-value problem

$$\left.\begin{aligned} -i\omega\nabla\cdot\left(\frac{\nabla\psi}{H}\right)+\hat{\boldsymbol{z}}\cdot\left(\nabla\psi\times\nabla\frac{f}{H}\right) = 0 \quad &\text{in } \mathscr{D}, \\ \psi = 0 \quad &\text{on } \partial\mathscr{D}, \end{aligned}\right\} \tag{2.3}$$

where $\mathscr{D}$ is the lake domain with the boundary $\partial\mathscr{D}$, through which no mass flux is assumed. This equation, derived for a homogeneous barotropic fluid, is approximately valid also in a two-layer baroclinic model provided that the upper layer is much thinner than the lower layer. This property evolves from the fact that the effect of the elevation of the interface on the barotropic processes is weak (Mysak *et al.* 1985). Rossby waves owe their existence to the term f/H in (2.3), i.e. to ∇f (planetary waves) or to ∇H (topographic waves). For lakes with a north to south length of less than 100 km the Coriolis parameter f may be assumed constant and only depth variations are important.

Since the topography H of the lake basin varies with respect to both dimensions, (2.3) is an inherently two-dimensional problem, which can be solved by separation of variables in only a few particular cases (Lamb 1932; Saylor *et al.* 1980; Mysak *et al.* 1985).

Real lakes often have an elongated, narrow shape and likewise, the trace of their thalweg may, on occasion, be substantially curved. This is so for many alpine lakes and suggests that we should try to employ this essentially one-dimensional feature. The use of a natural coordinate system, as shown in figure 1, is then appropriate; the curved s-axis follows the thalweg of the elongated lake and the n-direction is chosen to be straight and orthogonal to the s-direction. In such a curvilinear

coordinate system the horizontal gradient operator takes the form

$$\nabla = \frac{1}{J}\left(\frac{\partial}{\partial s}, \frac{\partial}{\partial n} J\right), \quad J = 1 - K(s)\, n, \tag{2.4}$$

where K denotes the curvature of the s-axis, see Pearson (1974). In this natural coordinate system the boundary-value problem (2.3) reads

$$\begin{aligned} \mathbf{D}\psi &= 0 \quad \text{in } \mathscr{D}, \\ \mathbf{B}\psi &= 0 \quad \text{on } \partial\mathscr{D}. \end{aligned} \tag{2.5}$$

with the definition of the differential and boundary operators $\mathbf{D}$ and $\mathbf{B}$, respectively

$$\left.\begin{aligned} \mathbf{D} &\equiv -\mathrm{i}\sigma\left(\frac{\partial}{\partial s}\frac{1}{JH}\frac{\partial}{\partial s} + \frac{\partial}{\partial n}\frac{J}{H}\frac{\partial}{\partial n}\right) + \frac{\partial}{\partial s}\left(\frac{1}{H}\right)\frac{\partial}{\partial s} - \frac{\partial}{\partial s}\left(\frac{1}{H}\right)\frac{\partial}{\partial n}, \\ \mathbf{B} &\equiv 1. \end{aligned}\right\} \tag{2.6}$$

$\sigma \equiv \omega/f$ is the non-dimensional frequency. Even in the simple case, when topographic waves in a straight ($J = 1$) infinite channel with an arbitrary cross-section are investigated, (2.5) confronts us with serious mathematical difficulties. Approximate solution techniques are required when more complicated topographies are to be studied. Analytical solutions can be constructed for piecewise exponential shelves (Mysak 1980) and weak parabolic depth profiles (Gratton 1983), but numerical (finite-element, finite-difference) methods are otherwise required. In the next section we present a semi-analytical approach that provides better physical insight than purely numerical methods generally do.

3. Method of Weighted Residuals

3.1. *Integrated representation of the equations*

Because in most cases problem (2.5) is not separable, we operate with a generalized method of separation – the Method of Weighted Residuals (MWR), see Finlayson (1972), Hutter & Raggio (1982) and Raggio & Hutter (1982).

Let $\{P_\alpha(s, n)\}$ be a convenient set of basis functions indexed by α, in terms of which the mass transport stream function $\psi(s, n)$ is expanded

$$\psi(s, n) = \sum_{\alpha=1}^{N} P_\alpha(s, n)\, \psi_\alpha(s) \equiv P_\alpha \psi_\alpha. \tag{3.1}$$

Each basis function is weighted by a residue function $\psi_\alpha(s)$ which is assumed not to depend on the transverse coordinate n. All functional dependence on n is now incorporated in the preselected basis functions P_α, a general form of separation. Expansion (3.1) represents the exact solution for a separable problem provided the basis functions $P_\alpha(s, n)$ are appropriately selected. For non-separable systems as (2.5) generally is, and for an arbitrary set $\{P_\alpha\}$ with $N < \infty$, expansion (3.1) is merely an approximation. Clearly, fast convergence is anticipated so that truncation of (3.1) for very small N may furnish a sufficiently accurate solution.

The integration of (2.5) with an arbitrary weighting function $\delta\phi(s, n)$ over the lake domain and along the shoreline, respectively, leads to the integral formulation of (2.5)

$$\int_{\mathscr{D}} (\mathbf{D}\psi)\, \delta\phi \, \mathrm{d}a = 0, \quad \oint_{\partial\mathscr{D}} (\mathbf{B}\psi)\, \delta\phi \, \mathrm{d}l = 0. \tag{3.2}$$

If (3.2) holds for any weighting function this is equivalent to (2.5) owing to the

fundamental lemma of the calculus of variation (Courant & Hilbert 1967). Expanding both the stream function (3.1) and the weighting function in terms of the sets $\{P_\alpha\}$ and $\{Q_\beta\}$, viz.

$$\delta\phi(s,n) = \sum_{\beta=1}^{N} Q_\beta(s,n)\,\delta\phi_\beta(s) \equiv Q_\beta\,\delta\phi_\beta.$$

and inserting these expansions into (3.2) yields

$$\int_{\mathscr{D}} (\mathbf{D}\,P_\alpha\psi_\alpha)\,Q_\beta\,\delta\phi_\beta\,\mathrm{d}a = 0, \quad \oint_{\partial\mathscr{D}} (\mathbf{B}\,P_\alpha\psi_\alpha)\,Q_\beta\,\delta\phi_\beta\,\mathrm{d}l = 0. \tag{3.3a, b}$$

The integration over the lake domain $\mathscr{D}$ can be split up into two integrations over either coordinates using $\mathrm{d}a = J\,\mathrm{d}n\,\mathrm{d}s$ for the area element in the natural coordinate frame. Further, the trivial form of the boundary operator $\mathbf{B} \equiv 1$ suggests the special choices

$$P_\alpha(s,B^\pm) = 0, \quad Q_\beta(s,B^\pm) = 0, \quad \text{for all } \alpha,\beta \tag{3.4}$$

such that the only contribution to (3.3*b*) arises from the ends of the lake.

Since the weighting functions are arbitrary, (3.3) can be replaced by

$$\left.\begin{aligned} \int_{n=B^-}^{n=B^+} (\mathbf{D}\,P_\alpha\psi_\alpha)\,JQ_\beta\,\mathrm{d}n = 0 \\ \psi_\alpha(s)|_{s=0,L} = 0 \end{aligned}\right\} \quad \alpha,\beta = 1,\ldots,N. \tag{3.5}$$

The residue functions ψ_α depend only on s and are therefore extracted from the integration by carefully accounting for the effect of the differential operator $\mathbf{D}$ on $\psi_\alpha(s)$. This procedure is performed in detail by Stocker & Hutter (1985). What results is the system

$$\left.\begin{aligned} \mathbf{M}_{\beta\alpha}\psi_\alpha = 0 \\ \psi_\alpha = 0 \end{aligned}\right\} \quad \alpha,\beta = 1,\ldots,N \quad \begin{cases} 0 < s < L, \\ s = 0, L, \end{cases} \tag{3.6}$$

with the matrix operator elements

$$\mathbf{M}_{\beta\alpha} = -\mathrm{i}\sigma\left[M^{00}_{\beta\alpha}\frac{\mathrm{d}^2}{\mathrm{d}s^2} + \left(\frac{\mathrm{d}M^{00}_{\beta\alpha}}{\mathrm{d}s} + M^{10}_{\beta\alpha} - M^{01}_{\beta\alpha}\right)\frac{\mathrm{d}}{\mathrm{d}s} + \left(\frac{\mathrm{d}M^{10}_{\beta\alpha}}{\mathrm{d}s} - M^{11}_{\beta\alpha} - M^{22}_{\beta\alpha}\right)\right]$$
$$-\,(M^{20}_{\beta\alpha} + M^{02}_{\beta\alpha})\frac{\mathrm{d}}{\mathrm{d}s} - \left(\frac{\mathrm{d}M^{20}_{\beta\alpha}}{\mathrm{d}s} + M^{12}_{\beta\alpha} - M^{21}_{\beta\alpha}\right) \quad (\alpha,\beta = 1,\ldots,N). \tag{3.7}$$

The matrix elements $M^{ij}_{\beta\alpha}$ represent quadrature formulae in the transverse direction, explicitly:

$$\left.\begin{aligned} M^{00}_{\beta\alpha} &= \int H^{-1}J^{-1}P_\alpha Q_\beta\,\mathrm{d}n, \\ M^{10}_{\beta\alpha} &= \int H^{-1}J^{-1}\frac{\partial P_\alpha}{\partial s}Q_\beta\,\mathrm{d}n, \quad & M^{01}_{\beta\alpha} &= \int H^{-1}J^{-1}P_\alpha\frac{\partial Q_\beta}{\partial s}\,\mathrm{d}n, \\ M^{20}_{\beta\alpha} &= \int H^{-1}\frac{\partial P_\alpha}{\partial n}Q_\beta\,\mathrm{d}n, & M^{02}_{\beta\alpha} &= \int H^{-1}P_\alpha\frac{\partial Q_\beta}{\partial n}\,\mathrm{d}n, \\ M^{11}_{\beta\alpha} &= \int H^{-1}J^{-1}\frac{\partial P_\alpha}{\partial s}\frac{\partial Q_\beta}{\partial s}\,\mathrm{d}n, & M^{22}_{\beta\alpha} &= \int H^{-1}J\frac{\partial P_\alpha}{\partial n}\frac{\partial Q_\beta}{\partial n}\,\mathrm{d}n, \\ M^{12}_{\beta\alpha} &= \int H^{-1}\frac{\partial P_\alpha}{\partial s}\frac{\partial Q_\beta}{\partial n}\,\mathrm{d}n, & M^{21}_{\beta\alpha} &= \int H^{-1}\frac{\partial P_\alpha}{\partial n}\frac{\partial Q_\beta}{\partial s}\,\mathrm{d}n, \end{aligned}\right\} \tag{3.8}$$

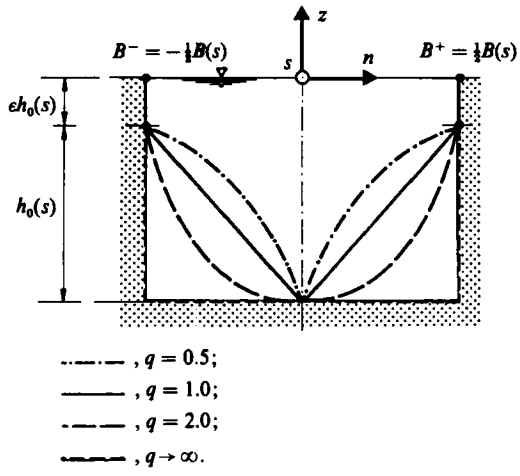

FIGURE 2. Cross-sectional depth profile of a symmetric channel.

whereby the integration is meant to extend from $B^-(s)$ to $B^+(s)$. For prescribed sets $\{P_\alpha\}$ and $\{Q_\beta\}$ the individual components $M^{ij}_{\beta\alpha}$ are known functions of s, which depend on the topography of the lake, on the curvature of its axis and on the shape of the shoreline.

Equations (3.6) form a system of coupled one-dimensional differential equations that replace the single two-dimensional boundary-value problem (2.5). These two formulations are presumed to be equivalent provided (i) the set of basis functions is complete in $[B^-, B^+]$ and (ii) $N = \infty$. The selected order N of the system sets a natural bound to the variability of the approximate solution as well as to its quality. At a first glance the MWR seems to leave us with a more complicated task. Finite-difference calculations, however, have indicated numerical difficulties such as slow convergence, particularly for complicated topographies and for large wave-numbers (Bäuerle 1986). This semi-analytical procedure may thus well prove advantageous in achieving a better physical understanding.

3.2. *Symmetrization*

More insight into the structure of the operator (3.7) is gained when the physical configuration exhibits symmetry with respect to the axis $n = 0$, as in figure 2. Such a symmetry may exist for channels and it often applies approximately for elongated, narrow lakes. The symmetrization is also motivated by the fact that solutions of the eigenvalue problem (2.3), found for circular and elliptic basins, indicate that the phase rotates counterclockwise and the stream function continuously changes its symmetry with respect to the symmetry axis of the lake. As a consequence a choice of only symmetric or only skew-symmetric basis functions will be a dubious approximation. Although the MWR need not be subject to this restriction we shall, for the purpose of studying channels and basins which have a symmetry axis, formulate problem (3.6) in a symmetrized version. To this end, the functions P_α, Q_β, J and J^{-1} are symmetrized by introducing the decompositions

$$\left.\begin{aligned} f(s,n) &= f^+(s,n) + f^-(s,n), \\ f^+(s,n) &= f^+(s,-n), \\ f^-(s,n) &= -f^-(s,-n). \end{aligned}\right\} \tag{3.9}$$

Here f stands for any of the above functions and the axis $n = 0$ is the centre of symmetry. This decomposition is applied to the matrix elements $M^{ij}_{\beta\alpha}$ in (3.8); the important result here is

$$\left.\begin{aligned} M^{00}_{\beta\alpha} &= M^{00++}_{\beta\alpha} + M^{00--}_{\beta\alpha} + M^{00-+}_{\beta\alpha} + M^{00+-} \quad (\alpha, \beta = 1, \ldots, N) \\ &= \int H^{-1}(J^{-1})^{+} P^{+}_{\alpha} Q^{+}_{\beta}\, \mathrm{d}n + \int H^{-1}(J^{-1})^{+} P^{-}_{\alpha} Q^{-}_{\beta}\, \mathrm{d}n \\ &\quad + \int H^{-1}(J^{-1})^{-} P^{-}_{\alpha} Q^{+}_{\beta}\, \mathrm{d}n + \int H^{-1}(J^{-1})^{-} P^{+}_{\alpha} Q^{-}_{\beta}\, \mathrm{d}n, \\ M^{20}_{\beta\alpha} &= M^{20-+}_{\beta\alpha} + M^{20+-} \\ &= \int H^{-1} \frac{\partial P^{-}_{\alpha}}{\partial n} Q^{+}_{\beta}\, \mathrm{d}n + \int H^{-1} \frac{\partial P^{+}_{\alpha}}{\partial n} Q^{-}_{\beta}\, \mathrm{d}n, \end{aligned}\right\} \tag{3.10}$$

with analogous expressions for $M^{22}_{\beta\alpha}$ and $M^{02}_{\beta\alpha}$ respectively. It has been assumed above that $H^{-} = 0$ (symmetric depth profile) and the integration is from $B^{-} = -\frac{1}{2}B(s)$ to $B^{+} = \frac{1}{2}B(s)$. Because the basis functions P_{α} and Q_{β} are decomposed according to (3.9) the expansion (3.1) of the solution $\psi(s, n)$ must be replaced by

$$\psi(s, n) = P^{+}_{\alpha}(s, n)\, \psi^{+}_{\alpha}(s) + P^{-}_{\alpha}(s, n)\, \psi^{-}_{\alpha}(s),$$

where the $\pm$ superscripts on ψ_{α} indicate merely affiliation to the individual $P^{\pm}_{\alpha}$. In vector notation the stream function reads

$$\boldsymbol{\psi} = (\psi^{+}_{1}, \ldots, \psi^{+}_{N}; \psi^{-}_{1}, \ldots, \psi^{-}_{N}) = (\boldsymbol{\psi}^{+}; \boldsymbol{\psi}^{-}),$$

and the matrices (3.10) take the form

$$\boldsymbol{M}^{00} = \begin{bmatrix} \boldsymbol{M}^{00++} & \boldsymbol{M}^{00-+} \\ \boldsymbol{M}^{00+-} & \boldsymbol{M}^{00--} \end{bmatrix}, \quad \boldsymbol{M}^{20} = \begin{bmatrix} \mathbf{0} & \boldsymbol{M}^{20-+} \\ \boldsymbol{M}^{20+-} & \mathbf{0} \end{bmatrix} \quad \text{etc.}$$

With this notation the differential equations (3.6) read

$$\left(-\mathrm{i}\sigma \begin{bmatrix} \mathbf{M}^{++} & \mathbf{M}^{-+} \\ \mathbf{M}^{+-} & \mathbf{M}^{--} \end{bmatrix} + \begin{bmatrix} \mathbf{0} & \mathbf{N}^{-+} \\ \mathbf{N}^{+-} & \mathbf{0} \end{bmatrix}\right) \begin{pmatrix} \boldsymbol{\psi}^{+} \\ \boldsymbol{\psi}^{-} \end{pmatrix} = \mathbf{0}, \tag{3.11}$$

with the matrix operators $\mathbf{M}$ and $\mathbf{N}$, the particular form of which is unimportant in the ensuing arguments.

The coupling of the solution vectors $\boldsymbol{\psi}^{+}$ and $\boldsymbol{\psi}^{-}$ is induced by the off-diagonal operators $\mathbf{M}^{-+}$, $\mathbf{M}^{+-}$ and $\mathbf{N}^{-+}$, $\mathbf{N}^{+-}$ respectively. The former are due to curvature and vanish when $K = 0$. The latter originate from the vector product in equation (2.3) and express the effect of the Coriolis force. The restriction to only symmetric basis functions reduces (3.11) to two decoupled sets of equations. This obviously corresponds to the claim that both terms of the sum of equation (2.3) be individually zero. On imposing the boundary condition this implies $\boldsymbol{\psi} \equiv 0$. It suggests that the approximate system (3.11) requires a set of basis functions containing both symmetric and antisymmetric functions if qualitatively correct results are to emerge.

4. Channel models

4.1. *Basic concept*

The suitability of the approximate model equations (3.6) deduced with the MWR is now tested using a straight, infinite and symmetric channel with a topography of the form

$$H(s,n) = h_0(s)\left(1+\epsilon-\left|\frac{2n}{B(s)}\right|^q\right), \tag{4.1}$$

where ϵ is a sidewall and q a topography parameter, see figure 2, which provides the possibility of modelling both concave ($q > 1$) and convex ($q < 1$) transverse depth profiles. The sidewall parameter ϵ has been introduced in order that all matrix elements (3.8) take finite values. The complete sets of basis functions $\{P_\alpha\}$ and $\{Q_\beta\}$ will be chosen to be identical (Galerkin procedure) with the symmetric and skew-symmetric parts reading

$$\left.\begin{aligned} P_\alpha^+(s,n) &= \cos\left(\pi(\alpha-\tfrac{1}{2})\frac{2n}{B(s)}\right) \\ P_\alpha^-(s,n) &= \sin\left(\pi\alpha\frac{2n}{B(s)}\right) \end{aligned}\right\} \quad (\alpha = 1,\ldots,N). \tag{4.2}$$

Here, P_α^+ and P_α^- arise in pairs; N thus characterizes a model consisting of $2N$ basis functions. These satisfy the boundary conditions (3.4) along the shoreline $n = \pm\frac{1}{2}B(s)$. Substituting (4.1) and (4.2) into (3.8) and assuming $B(s)$ to be constant it is seen that

$$\left.\begin{aligned} M_{\beta\alpha}^{00} &= B h_0^{-1} K_{\beta\alpha}^{00}, & M_{\beta\alpha}^{22} &= B^{-1}h_0^{-1} K_{\beta\alpha}^{22}, \\ M_{\beta\alpha}^{20} &= h_0^{-1} K_{\beta\alpha}^{20}, & M_{\beta\alpha}^{02} &= h_0^{-1} K_{\beta\alpha}^{02}, \end{aligned}\right\} \tag{4.3}$$

while the elements with the superscripts 10, 01, 11, 12 and 21 all vanish.

The dimension-free matrix elements $K_{\beta\alpha}^{ij}$ depend on ϵ and q and can be calculated numerically, see Stocker & Hutter (1985). The (non-symmetrized) matrix operator (3.7) takes the form

$$\mathbf{K} \equiv B h_0 \mathbf{M} = -\mathrm{i}\sigma\left[B^2 \boldsymbol{K}^{00}\frac{\mathrm{d}^2}{\mathrm{d}s^2} - B^2\left(h_0^{-1}\frac{\mathrm{d}h_0}{\mathrm{d}s}\right)\boldsymbol{K}^{00}\frac{\mathrm{d}}{\mathrm{d}s} - \boldsymbol{K}^{22}\right]$$
$$- B(\boldsymbol{K}^{20}+\boldsymbol{K}^{02})\frac{\mathrm{d}}{\mathrm{d}s} + B\left(h_0^{-1}\frac{\mathrm{d}h_0}{\mathrm{d}s}\right)\boldsymbol{K}^{20}. \tag{4.4}$$

This operator has constant coefficients whenever the depth-profile is constant or exponential with respect to the basin axis. For an infinite channel, however, we prefer $h_0(s) =$ constant. A carrier-wave ansatz

$$\boldsymbol{\psi} = (\boldsymbol{\psi}^+; \boldsymbol{\psi}^-) = \mathrm{e}^{\mathrm{i}ks/L}(c_1,\ldots,c_N; c_{N+1},\ldots,c_{2N}) = \mathrm{e}^{\mathrm{i}ks/L}\boldsymbol{c}, \tag{4.5}$$

with a dimensionless complex-valued wavenumber k, $\mathrm{Im}\,(k) \neq 0$ is meaningful in semi-infinite and finite channels, and a length L is then appropriate. With (4.4) and (4.5) the symmetrized form of (3.6) reduces to a system of algebraic equations

$$\boldsymbol{C}\boldsymbol{c} = 0,$$
$$\boldsymbol{C} = \begin{pmatrix} \sigma((rk)^2\boldsymbol{K}^{00++} + \boldsymbol{K}^{22++}) & -(rk)(\boldsymbol{K}^{20-+}+\boldsymbol{K}^{02-+}) \\ -(rk)(\boldsymbol{K}^{20+-}+\boldsymbol{K}^{02+-}) & \sigma((rk)^2\boldsymbol{K}^{00--}+\boldsymbol{K}^{22--}) \end{pmatrix}, \tag{4.6}$$

in which the aspect ratio parameter $r = B/L$ has been introduced. $\boldsymbol{C}$ is a $(2N \times 2N)$-matrix and depends on σ and k. Equation (4.6) admits a non-trivial solution vector $\boldsymbol{c}$ if and only if

$$\det \boldsymbol{C}(\sigma, k) = 0. \tag{4.7}$$

This characteristic equation forms the dispersion relation $\sigma(k)$ for topographic Rossby waves in a straight infinite channel. This is a polynomial equation of order $2N$ in $(rk)^2$ with real coefficients. For each frequency an Nth order model, therefore, yields $4N$ wavenumbers counting complex conjugates and pairs having opposite signs. So the model furnishes waves travelling in both directions of the channel.

Let k_γ $(\gamma = 1, \ldots, 4N)$ be a root of (4.7) corresponding to a frequency σ and let $\boldsymbol{c}_\gamma(c_{\alpha\gamma})$ be the associated eigenvector, (component) of (4.6). A general channel solution $\psi(s, n, t)$ can then be written as

$$\psi(s, n, t) = \mathrm{e}^{-\mathrm{i}\sigma f t} \sum_{\gamma=1}^{4N} \mathrm{e}^{\mathrm{i}k_\gamma s/L} d_\gamma \Bigg(\sum_{\alpha=1}^{N} P_\alpha^+(s, n)\, c_{\alpha\gamma} + \sum_{\alpha=N+1}^{2N} P_{\alpha-N}^-(s, n)\, c_{\alpha\gamma} \Bigg), \tag{4.8}$$

in which solutions belonging to individual k occur in a linear combination by an arbitrary complex vector $\boldsymbol{d}$, (d_γ). Representation (4.8) is an approximate solution in a straight infinite channel. For this particular configuration problem (2.5) is separable, the coefficients of the separated differential equation, however, are non-constant, and for very special topographies exact solutions can be obtained, see later and Gratton (1983). The MWR probably offers more freedom in modelling the channel topography, because improved accuracy can be obtained by higher-order models and convergence is expected.

4.2. *Dispersion relation*

Solutions of (4.7) may be plotted schematically for a first-order model $N = 1$ in a $(\mathrm{Re}(k), \mathrm{Im}(k), \sigma)$-coordinate system, see figure 3. This is a model which uses one symmetric and one skew-symmetric basis function of the form (4.2) and is of lowest possible order. Its graph is symmetric with respect to both axes $\mathrm{Re}(k) = 0$ and $\mathrm{Im}(k) = 0$. Three regimes 1, 2, 3 can be distinguished where the wavenumbers k take real, complex and purely imaginary values respectively. Table 1 gives the periods at which the individual regimes join for different topography and sidewall parameters. In regime 1 all wavenumbers k are real and, therefore, represent physically possible channel solutions. Typically for Rossby waves, for each frequency there exists a long and a short wave. It is worth noting that $\mathrm{Re}(k)$ can have both signs. This is in contrast to planetary Rossby waves which are due to the β-effect (Holton 1979) or Rossby waves on the continental shelf (Le Blond & Mysak 1978), the reason being that here H'/H changes sign in the channel. So, such configurations enable topographic Rossby waves to propagate in both directions. In either case, as an effect of the Coriolis force, the structure of the wave on the northern hemisphere is right-bound with respect to the direction of phase propagation. The dispersion relation (4.7) contains only even powers of σ such that either sign is mathematically reasonable. It turns out, however, that negative signs of σ result in a set of left-bound waves which propagate on the southern hemisphere where the Coriolis parameter f takes negative values. So, the sign of the timescaling factor f (Coriolis parameter) determines the sign of the non-dimensional frequency σ. The structure of the stream function depends upon the frequency range. Small frequencies favour periodic patterns along the channel. A critical wavenumber can be found at which no energy is transported along the channel. This corresponds roughly to wavelengths of about

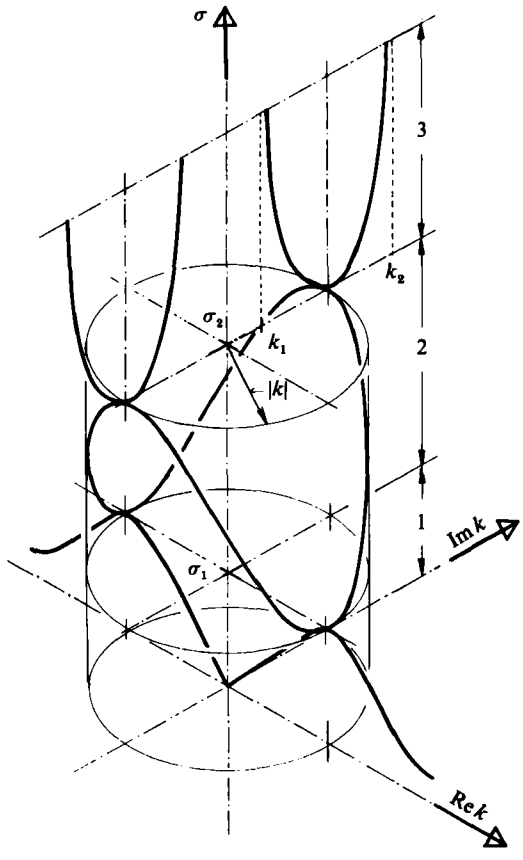

FIGURE 3. Schematic plot of the complex dispersion relation $\sigma(k)$ for an infinite channel with $\epsilon = 0.05$ and $q = 0.5$ in a first-order model. In regime 1, k is real; in regime 2, it is complex with the constant modulus $|k|$; and in regime 3, k is purely imaginary, taking asymptotic values k_1 and k_2 for large σ.

	$T_1[h]$		$T_2[h]$		$\|k\|$	
q	$\epsilon = 0.05$	$\epsilon = 0.10$	$\epsilon = 0.05$	$\epsilon = 0.10$	$\epsilon = 0.05$	$\epsilon = 0.10$
0.5	52.8	58.3	10.5	11.8	6.6	5.9
1.0	60.5	64.3	13.2	14.4	6.9	6.2
2.0	83.0	88.2	22.0	22.6	6.8	6.3
5.0	174	199	58.2	61.8	6.1	5.8

TABLE 1. Periods and corresponding wavenumbers in a first-order model, which separate the regimes, depending on topography and sidewall parameters q and ϵ respectively. The period T is calculated using $T = 16.9h/\sigma$ corresponding to 45° latitude. At T_1 no wave energy is transported.

half the channel width and the associated periods are listed in table 1. Waves with intermediate frequencies of order 1 have a mixed periodic–exponential structure and do not represent possible solutions in an infinite channel. At frequencies $\sigma > \sigma_2$ the solutions grow or decay exponentially. For later use, the union of the three regimes of the dispersion relation in figure 3 will be called a mode unit.

Let us proceed to the second-order model; it furnishes 8 wavenumbers to each

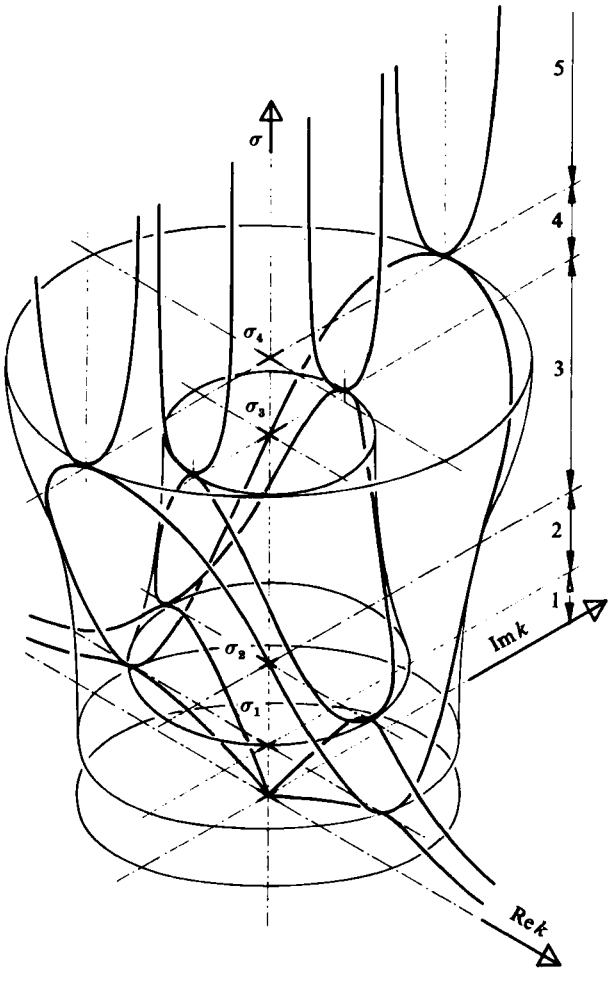

FIGURE 4. Schematic plot of the complex dispersion relation $\sigma(k)$ for an infinite channel with $\epsilon = 0.05$ and $q = 0.5$ in a second-order model. Five regimes with respect to σ can be differentiated.

frequency and its dispersion relation consists of two interlocking mode units, see figure 4. Thus there are now two branches with real, complex and imaginary k, respectively. The relative size of the mode units and their spatial position within the (k, σ)-coordinate system depend crucially upon the topography. The cylindrical surface of the first-order model degenerates to a smaller bell-shaped surface, i.e. $|k|$ now depends on the frequency. The second mode unit forms an outer shell, which here has the form of a cone. Physically possible solutions for the infinite channel exist in regime 1 for both mode units and in regime 2 only for the first mode unit. The qualitative shape of the dispersion relation for an Nth-order model can be guessed from figures 3 and 4. The modulus $|k|$ is plotted for a third-order model in figure 5, demonstrating clearly the addition of the next mode unit.

The MWR is an approximate approach and therefore convergence properties are expected. These are studied for the real branches of the dispersion relation. Figure 6 summarizes the results. The dispersion relation for $N = 3$ differs only slightly from that of the second-order model. The corrections of the second mode unit when

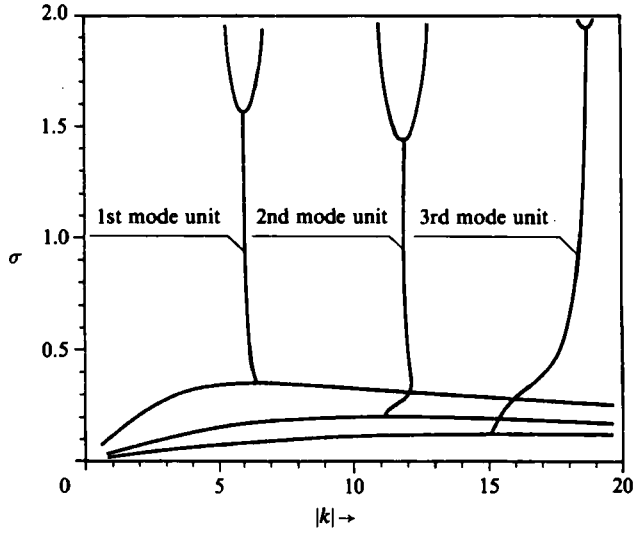

FIGURE 5. Modulus $|k|$ of the third-order dispersion relation for an infinite channel, $q = 0.5$; $\epsilon = 0.05$.

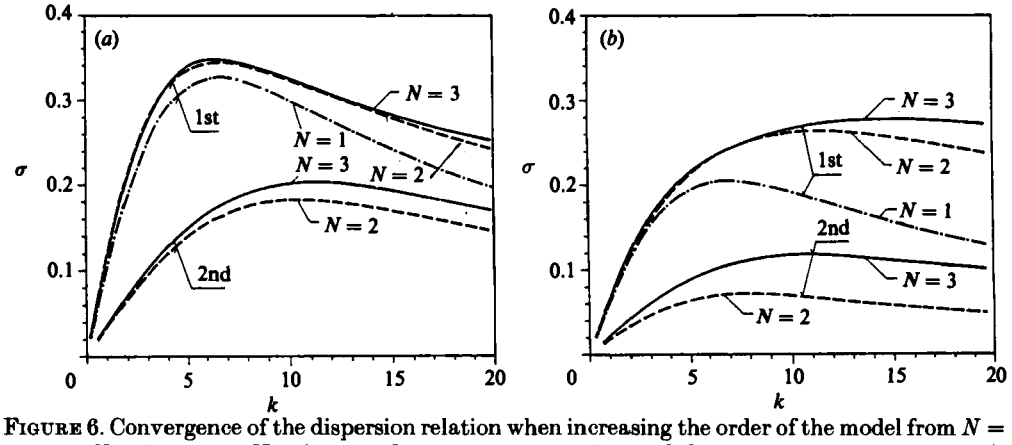

FIGURE 6. Convergence of the dispersion relation when increasing the order of the model from $N = 1$ (—·—), $N = 2$ (– – –) to $N = 3$ (——) for (*a*) convex ($q = 0.5$) and (*b*) concave ($q = 2.0$) topography, $\epsilon = 0.05$.

increasing the order are also shown; however, for a statement on convergence a 4th-order model would be needed. Convergence is not uniform in k, being better for small k than for large k; furthermore, it is better for convex ($q = 0.5$, figure 6*a*) than for concave ($q = 2.0$, figure 6*b*) topographies, which is unfortunate as the latter are more realistic. Further calculations have shown that the sidewall parameter ϵ does not influence convergence appreciably.

The quality of the MWR-approximation is more obvious when the dispersion relation is compared with that of an exact solution as in figure 7. The simple configuration of a straight channel leads to separable equations; these are easy to integrate provided the depth profile is piecewise exponential as indicated in the inset of figure 7. The dispersion relation $\sigma(k)$ evolves from the matching conditions of the stream function within the channel. As figure 7(*a*) demonstrates, the approximate dispersion curves calculated by the MWR applied to the same depth profile converge

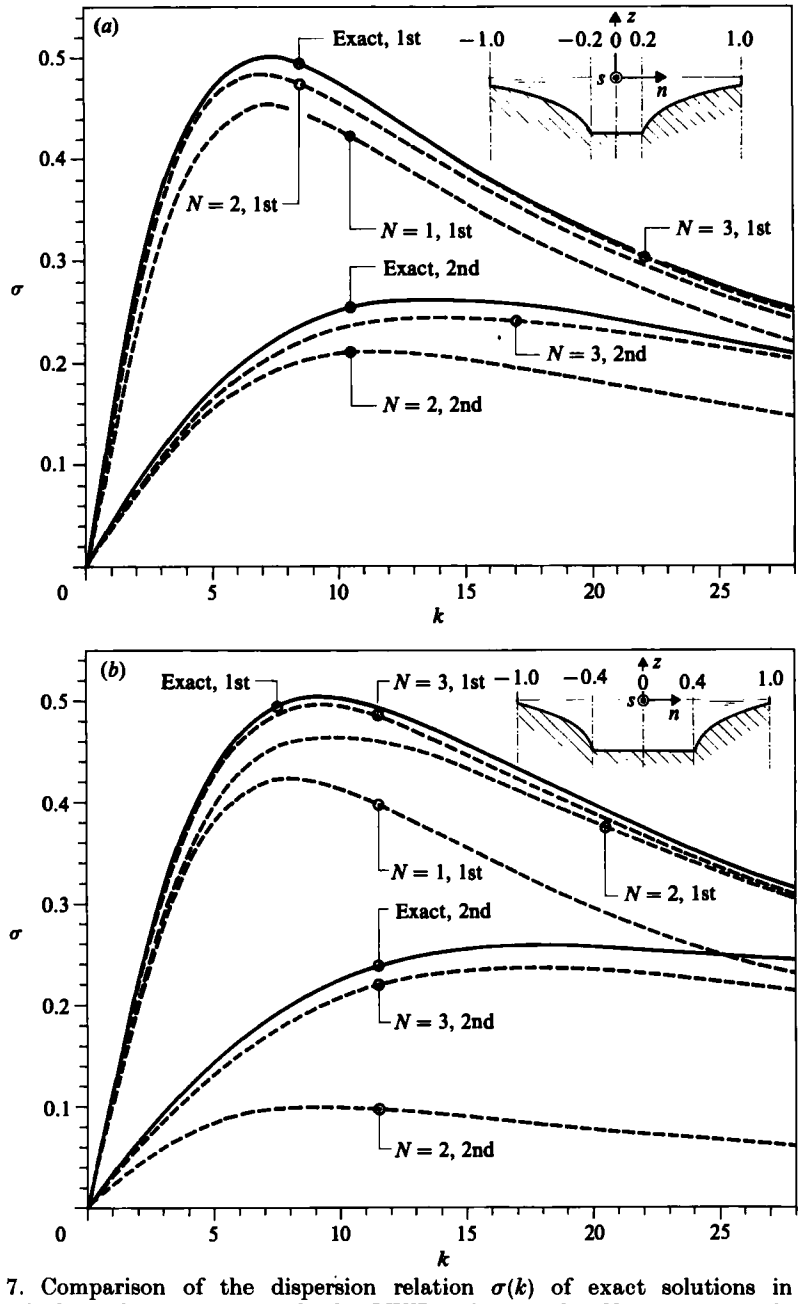

FIGURE 7. Comparison of the dispersion relation $\sigma(k)$ of exact solutions in a piecewise exponential channel (see inset) with the MWR solutions for $N = 1$, 2, 3 and the two first modes.

fast to the exact dispersion relation for the first mode. $N = 2$ already represents a satisfactory approximation within a few per cent. Convergence of the second mode is slower, as stated earlier. For steeper depth profiles, figure 7 (*b*), convergence is significantly slower and higher-order models may be required. But it also appears that the selected set of basis functions is not best for such configurations, as wave activity is concentrated at the shore.

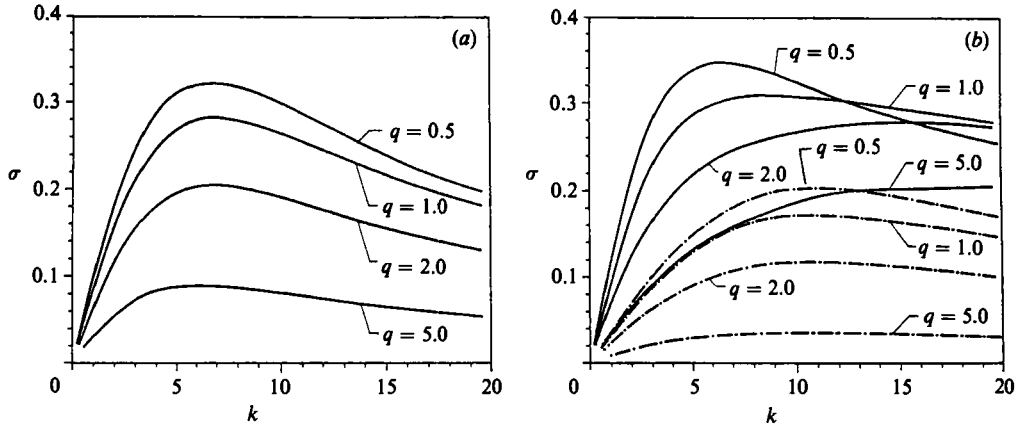

FIGURE 8. Effect of topography on the dispersion relation in a channel, ——, first mode; —.—, second mode, $\epsilon = 0.05$, (a) $N = 1$; (b) $N = 3$.

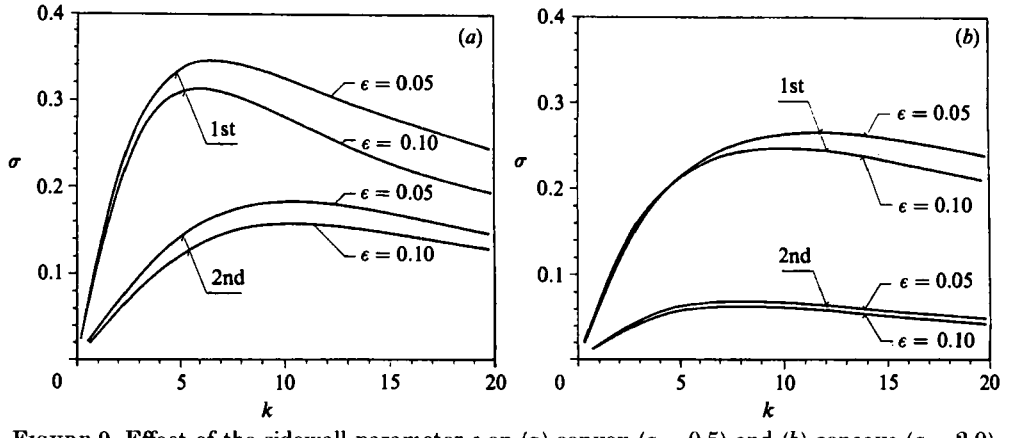

FIGURE 9. Effect of the sidewall parameter ϵ on (a) convex ($q = 0.5$) and (b) concave ($q = 2.0$) profiles in a second-order model.

Figure 8 shows the influence of the variation of the topography parameter q in a first- and third-order model. Comparison of figures 8(a) ($N = 1$) and 8(b) ($N = 3$) indicates clearly how sensitively the dispersion relation reacts to the topography. Generally, an increase of q shifts the dispersion relation to smaller frequencies; thus periods at the same wavenumber become longer. This could already be inferred from the fact that topographic gradients tend towards the boundary as q increases and the system will become weaker in its support of topographic Rossby waves.

Finally, figure 9 displays the dispersion relation of a second-order model for two different values of the sidewall parameter ϵ and for both convex and concave depth profiles. The latter are less affected by ϵ than the former because all convex profiles of the form (4.1) join the sidewall horizontally. The sidewall effect consists of a decrease of the frequency with growing ϵ, which might be expected since topography variations are reduced thereby.

The question of whether k_0 at which $\partial\sigma/\partial k = 0$ exists for all topographies or wanders off to infinity is of some practical significance. If situations with $k_0 = \infty$ existed, closed basin solutions could not be constructed. Figure 10 displays k_0 against the topography parameter q for a few values of ϵ. Whereas for convex profiles k_0

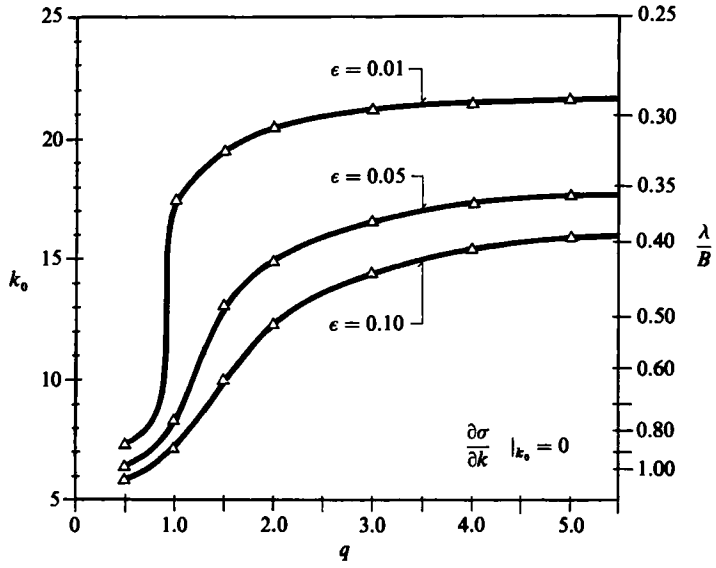

FIGURE 10. Plot of the critical wavenumber k_0, where the group velocity is zero, as a function of topography and sidewall parameter for the first mode in a third-order model.

hardly depends on the sidewall parameter ϵ this is not so for concave profiles: a decrease of ϵ conspicuously increases the values of k_0. Alternatively, for large topography parameters k_0 is fairly independent of q. It is evident that models with very small sidewall parameters have very large critical wavenumbers and it appears that the dispersion relation becomes single valued with respect to σ. Such a conclusion is not appropriate, as can be demonstrated following Huthnance (1975) with modifications.

4.3. *Channel solutions*

Equation (4.8) represents a general solution in a straight, infinite channel with arbitrary cross-section. ψ is a complex-valued function and so both real and imaginary parts are physically reasonable solutions. However, as can be easily shown, they differ only by a spatial or temporal phase shift. Rather than considering general solutions such as (4.8), we only investigate solutions to particular wavenumbers.

Figure 11 exhibits the quality of the approximate solutions. Calculations have revealed that for a convex topography solutions converge rapidly for a wide range of wavenumbers, a result which is in accord with the observations above. For a concave topography ($q = 5.0$, figure 11) the third-order solution is an acceptable approximation when $k = 2$ (figure 11*a*); however, as figure 6 has already suggested, convergence for higher wavenumbers is slower (figure 11*b*). Convergence is obviously also influenced by the choice of basis functions and it seems that the trigonometric functions are an appropriate set for small wavenumbers. It was a straightforward choice and made for analytical and computational simplicity. There may, however, be other complete sets, fulfilling the boundary conditions, which provide better results in some special cases. With the (sin, cos)-set the exact transverse functional dependence is well modelled for fundamental modes, with not too large wavenumbers and small topography parameters.

Figure 12 analyses the effect of the cross-channel topography on the stream

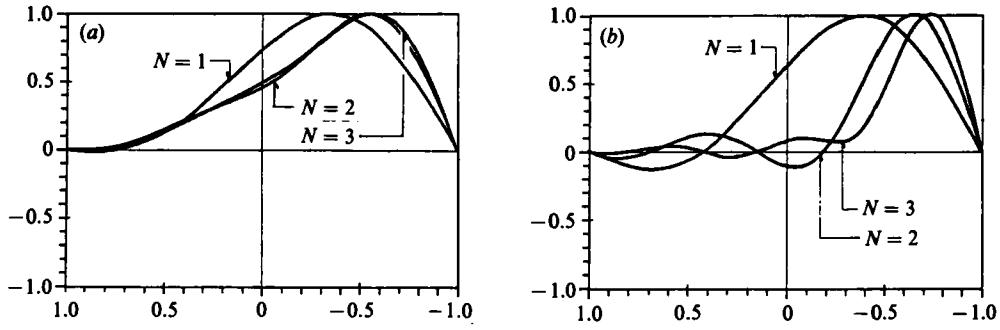

FIGURE 11. Convergence properties of the stream function of the first mode scaled to a maximum value 1.0. The view is in the positive s-direction into which the phase propagates in a right-bound way. The sidewall parameter $\epsilon = 0.05$ is selected, $q = 5$, (*a*) $k = 2$; (*b*) $k = 10$.

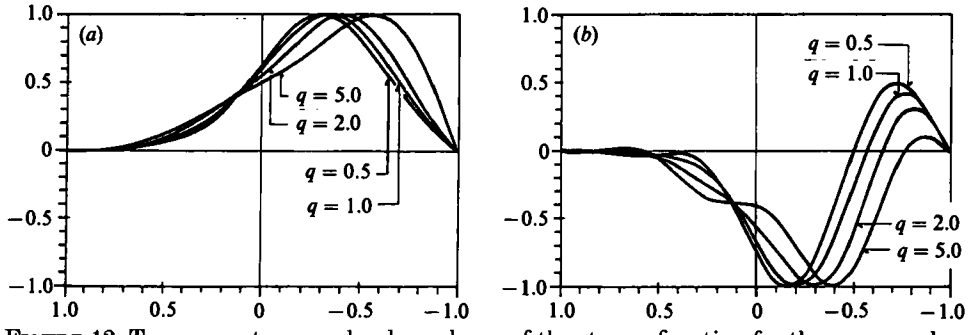

FIGURE 12. Transverse topography dependence of the stream function for the wavenumber $k = 2$ and the first two modes. $N = 3$, (*a*) first mode; (*b*) second mode.

function using q as a parameter. In view of the previous results, a third-order model is anticipated to be sufficiently accurate. The effect for small wavenumbers ($k = 2$) and the first mode (figure 12*a*) is comparatively weak: wave activity is slightly shifted towards the right boundary for increasing topography parameters. Larger wavenumbers enhance this effect.

For the second-mode solutions an increase of the topography parameter again causes a shift of the ψ-surface towards the right boundary, see figure 12*b*. The right-most crest, however, is weakened and for larger topography parameters the main activity is in the middle crest.

Evidently, the transverse structure of topographic Rossby waves also depends strongly on the wavenumber k. This effect is comparable in magnitude with that of the topography. Figure 13 demonstrates this for both types of topographies and the first two modes.

An increase of k generally shifts the stream function towards the right shoreline. The effect is large (small) for profiles with large (small) q particularly for the first-mode unit. Topography and wavenumber effect, therefore, act in the same way. These properties have not been clearly demonstrated in previous work. Suffice it to state that they have important practical bearings when mooring sites are projected.

4.4. *Velocity profiles*

The general channel solution (4.8) which satisfies the homogeneous system (3.6) is determined up to a constant factor. In order to compare different velocity profiles

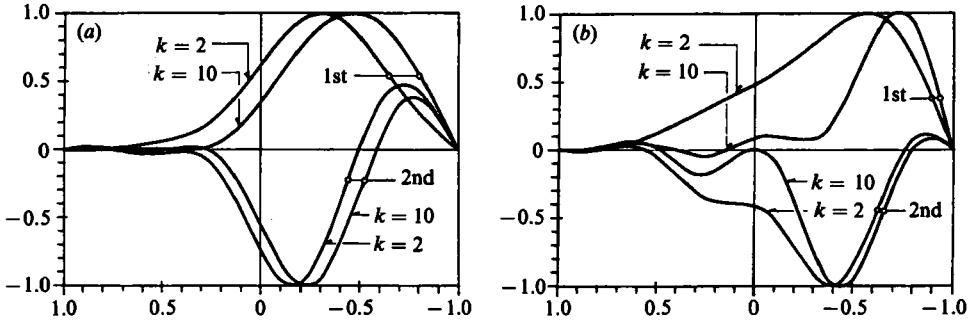

FIGURE 13. Wavenumber effect on the stream function for (*a*) convex ($q = 0.5$) and (*b*) concave ($q = 5.0$) topography, $\epsilon = 0.05$ and the first two modes of a third-order model.

this constant should be fixed by using a further criterion. It seems reasonable to scale the occurring wave patterns by normalizing the free constant such that the global kinetic energy content is constant. (There is no potential energy for topographic Rossby waved in a rigid-lid formulation.) Here, the problem is posed in terms of the barotropic mass transport stream function and a solution yields information about a depth-averaged velocity field. This allows the calculation of only a *lower limit* of the kinetic energy content.

The kinetic energy per unit mass that is contained in an infinitesimal volume is

$$\mathrm{d}E^3_{\mathrm{kin}} = \tfrac{1}{2}(u^2+v^2)\,J\,\mathrm{d}n\,\mathrm{d}s\,\mathrm{d}z, \tag{4.9}$$

in which the velocity components u, v can be expressed in terms of the stream function with (2.2), and for straight channels $J = 1$.

A minimum average energy density is obtained by integrating (4.9) across the channel axis and over the vertical, then operating with

$$\lim_{T\to\infty}\frac{1}{T}\int_0^T \mathrm{d}t, \quad \lim_{L\to\infty}\frac{1}{L}\int_0^L \mathrm{d}s$$

and dividing by the cross-sectional area. It then reads

$$E_{\mathrm{kin}} = \frac{1}{1+\epsilon-\dfrac{1}{q+1}}\int_{-1}^{1}\frac{\mathrm{d}y}{H}\left(k_\gamma^2|P^+_\alpha c_{\alpha\gamma}+P^-_{\alpha-N}c_{\alpha\gamma}|^2+4|P^{+\prime}_\alpha c_{\alpha\gamma}+P^{+\prime}_{\alpha-N}c_{\alpha\gamma}|^2\right), \tag{4.10}$$

where $y = 2n/B$ and $' = \mathrm{d}/\mathrm{d}y$. When the stream function is scaled by $1/(E_{\mathrm{kin}})^{\frac{1}{2}}$ each wave contains the same kinetic energy. This enables comparison of the strength and structure of a wave pattern as a response to a given energy input.

Figure 14 displays the amplitude distributions of the along-shore and cross-channel velocity profiles for the first mode at $k = 10$ and $\epsilon = 0.5$ for four different topography parameters q. Sign changes correspond to a phase shift of 180°. Evidently, the u-component indicates a strong right-bounded coastal jet which is well known in forced circulation models (Simons 1980). Its strength depends upon the parameters q and ϵ. An increase of q lowers the absolute value of the velocity components considerably.

We have also observed, and figure 14 provides partial corroboration, that convergence of at least u is slower than that for the stream function. The reason is, of course, differentiation. Deviations of the computed velocity profiles from what they should be occur at the left shoreline (figures 14*a* and 15*a*).

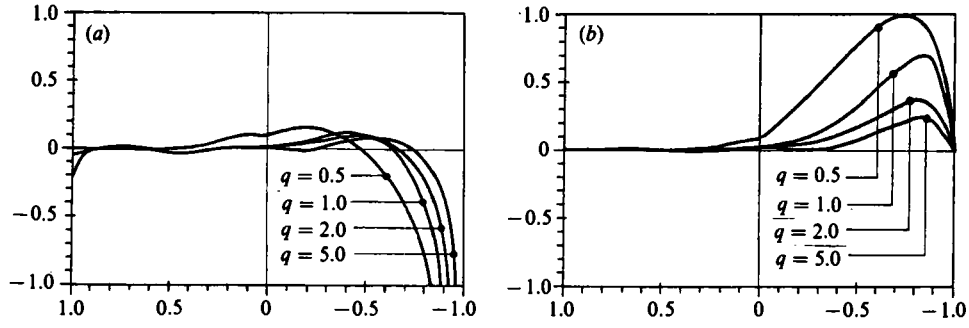

FIGURE 14. Transverse topography dependence of the depth-averaged velocity components (*a*) u (along-channel) and (*b*) v (across-channel) for $N = 3$, $k = 10$, $\epsilon = 0.05$ and the first mode. All profiles are scaled such that the kinetic energy contents are comparable.

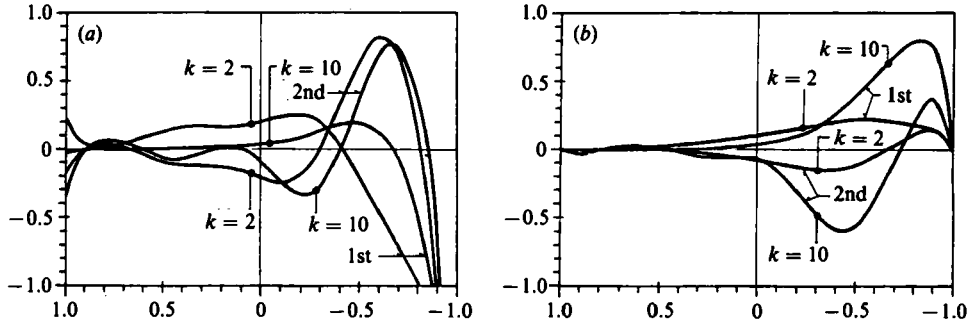

FIGURE 15. Wavenumber effect of the depth-averaged velocity components for $q = 2.0$, $\epsilon = 0.05$ and the first two modes of a third-order model, (*a*) u-component; (*b*) v-component.

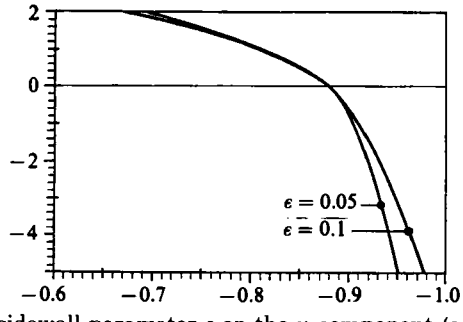

FIGURE 16. Effect of the sidewall parameter ϵ on the u-component (along-channel) at $k = 10$ and with $q = 2.0$. Because the profiles differ from each other only at the right shore this domain is enlarged. $N = 3$, first mode.

Figure 15 illustrates the wavenumber effect for the case $q = 2$ (parabolic) and $\epsilon = 0.05$. With growing wavenumber, activity in the u-component shifts to the right shore and, correspondingly, activity diminishes on the left part of the channel. Alternatively, cross-channel components grow with increasing k. Therefore long waves exhibit particle motion which is mostly along the channel axis. Shorter waves with wavelengths smaller than about a channel width have velocities of comparable order in both directions. These properties also hold for the second mode.

As anticipated when introducing the sidewall parameter ϵ its effect on the

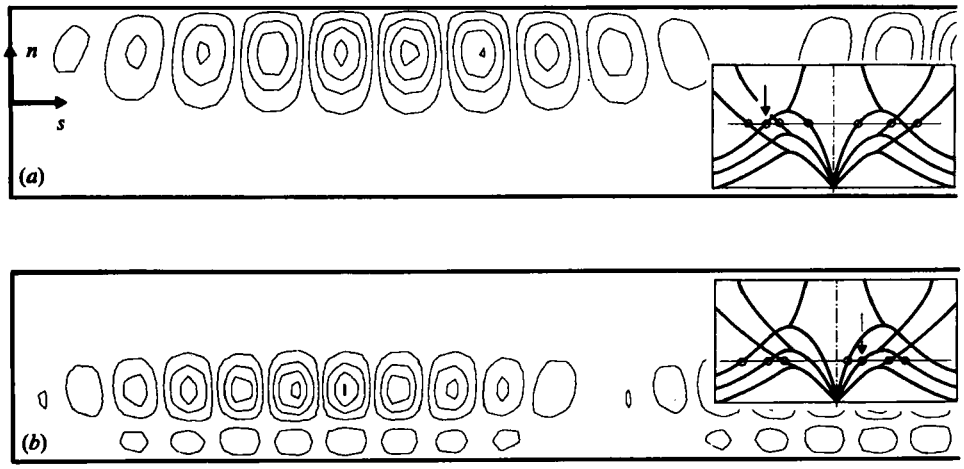

FIGURE 17. ψ-contour lines of a reflection of topographic waves at a vertical wall. The insets explain the composition of the reflection pattern with ●, incident wave and ○, reflected wave. The selected parameters are $N = 3$, $\epsilon = 0.05$, for (*a*) $q = 1.0$, $\sigma = 0.305$ and (*b*) $q = 0.5$, $\sigma = 0.202$.

depth-averaged velocity profiles is very weak and only recognizable in the u-component and close to the shoreline. Figure 16 demonstrates this for a channel with parabolic depth-profile. Velocity profiles differ from each other only very close to the right boundary. The u-component of the velocity vector there is directly governed by ϵ and its absolute value increases as ϵ approaches zero.

The above results can be used to answer questions which arise when topographic wave motion in channels or narrow elongated lakes is to be detected and recorded. Scrutiny of the wavenumber dependence shows that, in order to record the first mode on a concave topography ($q = 2.0$, $q = 5.0$), the mooring system is best placed within a domain that is 0.05 B to 0.1 B (B is the channel width) away from the shore. Then, both velocity components are of comparable magnitude and a whole range of wavenumbers can be detected with a velocity vector which turns clockwise. The second mode can most likely be detected within a domain which is 0.1 B to 0.2 B away from the shore. For a proper test of the wave structure two moorings at the same side of the channel are desired.

4.5. *Reflection of topographic waves*

A property of the MWR is that it furnishes solutions with complex wavenumbers k in a natural way. This suggests that solutions of the form (4.8) can be found which represent the situation of reflected topographic Rossby waves in a channel. The idea is to superpose several waves with the same frequency: an incident and a reflected wave, both with real k, and some waves with $\mathrm{Im}(k) > 0$ which are important only in a boundary zone where the reflection is induced. The superposition satisfies the boundary condition $\psi = 0$ (no flux) at the reflecting wall.

Consider a semi-infinite channel $s \geqslant 0$ with a wall at $s = 0$. One particular wave mode forms the incident wave; its phase and group velocities may both propagate towards the wall as shown for a first-mode response in figure 17(*a*). Alternatively, group and phase velocities may have different directions as in the second-mode response of figure 17(*b*). 'Incident' means that the energy propagates towards the wall and all the reflected waves need to have opposite energy propagation. Then, the

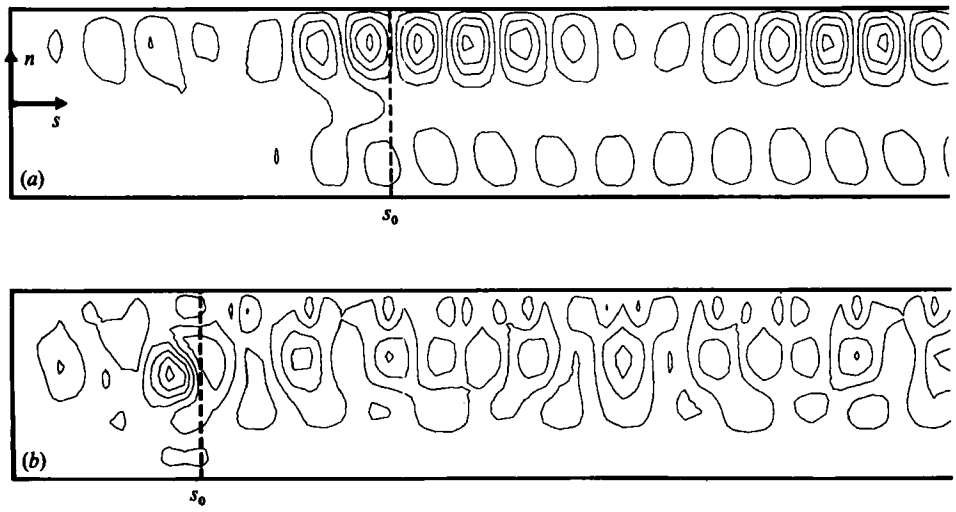

FIGURE 18. Reflection pattern in a composed channel. For $0 < s < s_0$ the depth varies exponentially along the axis whereas it is constant for $s > s_0$. This connects the isobaths of both channel domains $n > 0$ and $n < 0$ and enables wave energy to leak into the opposite domain in the course of reflection. The selected parameters are $\epsilon = 0.05$, for (*a*) $N = 2$, $q = 2.0$, $\sigma = 0.260$, $s_0 = 2.0$ and (*b*) $N = 3$, $q = 0.5$, $\sigma = 0.200$, $s_0 = 1.0$.

superposition and the determination of the compound solution is unique. We have found that the largest portion of the reflected energy lies in the mode with the corresponding wavenumber belonging to the same branch of the dispersion relation (indicated by arrows in the insets of figure 17).

Therefore, the mode with the negative of the incident wavenumber is hardly excited, and reflection causes primarily a shift of wavenumber rather than a change of its sign. As a consequence, wave activity remains at the side of the incident wave. What results is a beat pattern with its first 'calm' area at approximately $2\pi B/|k_{\text{in}} - k_{\text{out}}|$ away from the wall. Within such a cell a phase propagation in the same direction as the incident wave can be observed, and the structure of this cell depends on the two main wavenumbers k_{in} and k_{out}. If these differ markedly from each other rather local and small-scale patterns emerge. This may hint that elongated basins scarcely show fundamental topographic waves with basin-wide structure unless they have a very special bathymetry (Ball 1965; Mysal *et al.* 1985). Finite-element calculations of Trösch (1984) revealed similar results. It is characteristic of these basin-wide wave structures that the phase rotates counterclockwise around the basin. Figure 17 demonstrates that such a rotation does not occur in this simple configuration.

So, in an elongated basin the depth-profile at the very end is of crucial importance for the structure of the reflection. In the case of a vertical wall the lines of constant f/H (isobaths) along which the waves can propagate terminate at the channel end and apparently prevent the wave from changing channel side.

The differential equations (4.4) keep constant coefficients provided that h_0 varies exponentially along the channel axis. Therefore let the channel be composed of two sections. Close to the barrier, for $0 < s < s_0$, the depth increases exponentially with s: $h_0(s) \doteq \epsilon h_0 \exp((s/s_0)\log(1+1/\epsilon))$; for $s > s_0$ it is constant. The isobaths now no longer intersect the wall but are $\subset$-shaped. Figure 18 shows solutions for such a configuration; a significant difference to figure 17 is observed. Now, there is wave

2:1 basin	$N = 1$	$N = 2$	$N = 3$
$q = 0.5$	0.314	0.335	0.337
	0.292	0.316	0.317
	0.264	0.293	0.295
$q = 2.0$	0.198	0.260	0.274
	0.186	0.254	0.271
	0.169	0.246	0.267
$q = 5.0$	0.087	0.167	0.208
	0.081	0.163	0.206
	0.073	0.158	0.202

TABLE 2. First eigenfrequencies σ, $r = 0.5$, i.e. 2:1 basin, and $\epsilon = 0.05$ in a simple lake model. There is always a pair of eigenfrequencies differing from each other by less than 1 % and the table shows only one of them.

q	$r = 0.5$	$r = 0.4$	$r = 0.3$	$r = 0.2$
0.5	0.335	0.337	0.339	0.341
1.0	0.303	0.304	0.304	0.305?
2.0	0.260	0.260	0.261	0.261
5.0	0.167	0.167	0.167	0.168?

TABLE 3. The first eigenfrequency in a second-order model for various aspect ratios r and topography parameters q, $\epsilon = 0.05$. Question marks indicate computational difficulties.

activity also in the opposite half of the channel corresponding to the negative of the incident wavenumber. This amounts to a weak leakage of wave energy by reflection into the other channel domain (figure 18*a*). However, probably owing to the non-smoothness of the isobaths, it is comparatively weak and most of the reflected wave activity remains on the incident side.

Figure 18(*b*) shows a reflection pattern of lower frequency, k_{in} and k_{out} lie farther apart and therefore more local and complicated structures result. Moreover, at the beginning of the reflecting shelf ($s \approx s_0$) wave activity is intensified. These specific results demonstrate that the global wave pattern is very sensitive to the basin shape and the depth profile at the channel end. Further studies are needed.

5. Lake models

As there exist $4N$ independent channel solutions of the form (4.8) in an Nth order model, these can be superposed to a lake solution. A crude lake model is obtained by inserting vertical walls at two positions $s = 0$ and $s = L$. There, the stream function ψ must vanish,

$$\left.\begin{aligned} \sum_{\gamma=1}^{4N} c_{\alpha\gamma} d_\gamma &= 0 \\ \sum_{\gamma=1}^{4N} \mathrm{e}^{\mathrm{i}k_\gamma} c_{\alpha\gamma} d_\gamma &= 0 \end{aligned}\right\} \quad (\alpha = 1, \ldots, 2N), \tag{5.1}$$

This homogeneous system has a non-trivial solution provided that its determinant is zero. Equations (5.1) select the eigenfrequencies of the system which depend on the bathymetry given by r, q and ϵ. Periodic lake solutions exist only for $0 < \sigma < \sigma_0$,

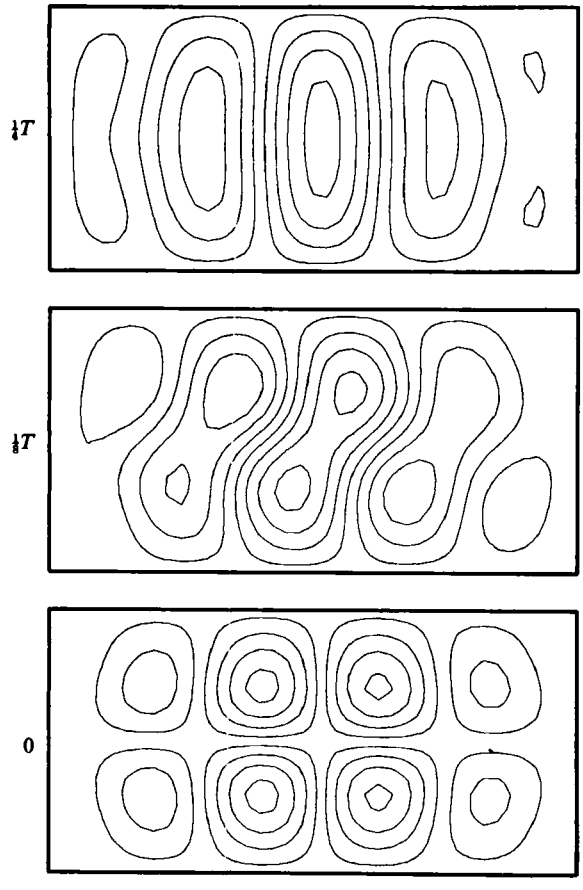

FIGURE 19. Lake solution in a 2:1 basin plotted for three different times through a quarter of a period T, using $N = 2$, $q = 0.5$, $\epsilon = 0.05$ and $\sigma = 0.335$. Wave activity is strongest in the middle of the basin and damped at both ends.

where σ_0 denotes the maximum frequency of the real branch of the first-mode unit. Consequently, frequencies decrease appreciably when the topography parameter q increases. This effect is demonstrated in table 2 which compares the first eigenfrequencies of different models. For a parabolic depth profile a third-order model offers adequate estimates of the eigenfrequencies. A parameter study reveals that the topography parameter q influences the eigenfrequencies much more than do r or even ϵ, see table 3. However, for small r, $r < 0.2$, convergence is more difficult to obtain, the reason being that large contributions of modes with complex wavenumbers k, $\mathrm{Im}(k) > 0$ arise. The results of a series of reflected topographic Rossby waves suggest that Ball-type solutions, i.e. phase lines rotating around the basin, are not observed. Figure 19 shows a series of pictures of a lake solution in a 2:1 basin. The influence of the vertical walls is obvious in that wavecrests approaching them die out. As mentioned, the fundamental mode does not resemble Ball-type behaviour; rather, the wave pattern exhibits a local structure. As the eigenfrequencies decrease the local character becomes stronger, but there is still a right-bounded phase propagation. Figure 20 presents some specific lake solutions for $N = 2$ and $N = 3$ models. Figure

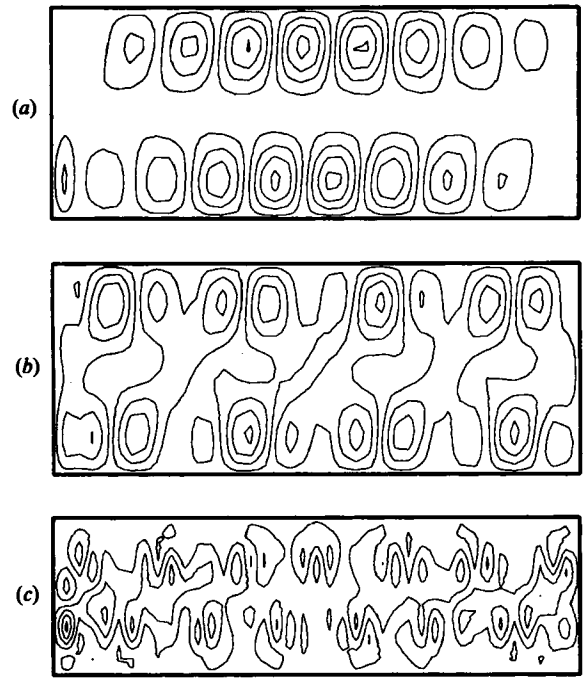

FIGURE 20. Stream function of three examples of solutions in a 'crude' lake model. The parameters are

	N	r	q	ϵ	σ
(a)	2	0.4	2.0	0.05	0.260
(b)	2	0.4	2.0	0.05	0.244
(c)	3	0.3	0.5	0.05	0.120

20(a) is similar to a compound channel solution of the form of figure 17(a). Wave patterns in $n > 0$ and $n < 0$ seem not to interact, whereas for a higher mode (figure 20b) flow across the channel is observed. Figure 20(c) displays the stream-function pattern of a very complex solution with strong local structure. It seems that Ball-type solutions are rather unlikely to exist in natural, not very smoothly shaped basins.

Calculations further showed that for small aspect ratios r the system (5.1) is very difficult to handle. The smaller r is, the larger are all $|\mathrm{Im}(k)|$, and terms of (5.1b) become dominant: the smallest inaccuracies in the eigenvector d_γ are fatal because of their amplification in the terms proportional to $e^{|k_\gamma|}$. A remedial measure might be a superposition of two semi-channel solutions displaced with respect to each other by a length L.

6. Conclusions

We have demonstrated that the MWR is an effective tool in deducing classes of approximate one-dimensional models for topographic Rossby waves. This has not been analysed in detail by finite-element of finite-difference methods, and these latter

techniques are rather time consuming on a computer and results are more easily accessible by our reduced models.

By increasing the order N of the model, both the dispersion relation and the stream function demonstrated convergent features. For a special channel this was consolidated by comparison of our approximate solutions with exact analytical solutions. $N = 3$ proved to furnish a practicable model for all wavenumbers, and for a low wavenumber domain even the cruder model ($N = 2$) produced results that were reasonably close to those of exact solutions. Dispersion relations and stream functions indicate conspicuous topography and wavenumber dependencies. Additionally, the dispersion relation exhibited domains with complex wavenumbers. These correspond to non-periodic, exponentially decaying modes. With these modes, the problem of topographic wave reflection in a semi-infinite channel could be solved. This analysis demonstrated that the bathymetry at the reflecting wall is of crucial importance and governs the structure of the global pattern. Wave energy can only leak into the opposite channel domain when isobaths are continuous, and the amount of this leakage depends on the order of continuity.

An Nth-order model yields enough solutions to combine them and satisfy no-flux conditions at two different positions. Analysis of a 'crude' lake model showed that the eigenfrequencies depend strongly on the depth profile of the channel. Wave patterns in elongated lakes showed a more complicated and local structure than expected. Solutions are very sensitive to round-off errors when r is small and a modified procedure must be found to construct reliable results.

Our model also offers the possibility of solving topographic wave problems in even more complex domains where $h_0(s)$ in (4.1) varies with position. In this case the matrix operator $\mathbf{K}$ in (4.4) no longer has constant coefficients and an algebraic procedure cannot be applied. The operator $\mathbf{K}$ acting on ψ then forms a system of coupled differential equations which must be solved by a numerical two-point boundary-value solver. These and other open questions are the subject of further investigations.

The artwork was done by C. Bucher and F. Langenegger and M. Staub typed various versions.

Note added in proof. In work still under progress and shortly to be submitted we describe topographic wave motion in closed basins in much greater detail. In rectangular basins with depth variation along the thalweg we also found solutions as shown in figures 19 and 20, but equally detected Ball-type modes and modes with wave activity restricted to the long ends of the rectangle.

REFERENCES

BÄUERLE, E. 1986 Eine Untersuchung über topographische Wellen in einem Kanalmodell. *Mitteilungen der Versuchsanstalt für Wasserbau, Hydrologie und Glaziologie*, ETH Zürich No. 83.

BALL, F. K. 1965 Second class motions of a shallow liquid. *J. Fluid Mech.* **23**, 545–561.

CHRYSTAL, G. 1904 Some results in the mathematical theory of seiches. *Proc. R. Soc. Edin.* **25**, 328–337.

CHRYSTAL, G. 1905 Some further results in the mathematical theory of seiches. *Proc. R. Soc. Edin.* **25**, 637–647.

COURANT, R. & HILBERT, D. 1967 *Methoden der mathematischen Physik*, vols 1 and 2. Springer.

DEFANT, A. 1918 Neue Methode zur Ermittlung der Eigenschwingungen (seiches) von abgeschlossenen Wassermassen (Seen, Buchten, usw.). *Ann. Hydrogr. Berlin*, **46**.

FINLAYSON, B. A. 1972 *The Method of Weighted Residuals and Variational Principles*. Academic.

GRATTON, Y. 1983 Low frequency vorticity waves over strong topography. Ph.D. thesis, Univ. of British Columbia.

HOLTON, J. R. 1979 *An Introduction to Dynamical Meteorology*, 2nd edn. Academic.

HUTHNANCE, J. M. 1975 On trapped waves over a continental shelf. *J. Fluid Mech.* **69**, 689–704.

HUTTER, K. & RAGGIO, G. 1982 A Chrystal-model describing gravitational barotropic motion in elongated lakes. *Arch. Meteorol. Geophys. Bioclimatol.* A, **31**, 361–378.

HUTTER, K., SALVADE, G. & SCHWAB, D. J. 1983 On internal wave dynamics in the northern basin of the Lake of Lugano. *Geophys. Astrophys. Fluid Dyn.* **27**, 299–336.

LAMB, H. 1932 *Hydrodynamics*, 6th edn. Cambridge University Press.

LE BLOND, P. H. & MYSAK, L. A. 1978 *Waves in the Ocean*. Elsevier.

MYSAK, L. A. 1980 Recent advances in shelf wave dynamics. *Rev. Geophys. Space Phys.* **18**, 211–241.

MYSAK, L. A., SALVADE, G., HUTTER, K. & SCHEIWILLER, T. 1985 Topographic waves in an elliptical basin, with application to the Lake of Lugano. *Phil. Trans. R. Soc. Lond.* A **316**, 1–55.

PEARSON, C. E. 1974 *Handbook of Applied Mathematics*. VNR.

PEDLOSKY, J. 1979 *Geophysical Fluid Dynamics*. Springer.

RAGGIO, G. & HUTTER, K. 1982 An extended channel model for the prediction of motion in elongated homogeneous lakes. *J. Fluid Mech.* **121**, 231–299.

SAYLOR, J. H., HUANG, J. S. K. & REID, R. O. 1980 Vortex modes in southern Lake Michigan. *J. Phys. Oceanogr.* **10**, 1814–1823.

SIMONS, J. T. 1980 Circulation models of lakes and inland seas. *Can. Bull. Fisheries and Aquatic Sci.* No. 203.

STOCKER, T. & HUTTER, K. 1985 A model for topographic Rossby waves in channels and lakes. *Mitteilungen der Versuchsanstalt für Wasserbau, Hydrologie und Glaziologie, ETH Zürich*, No. 76.

TAYLOR, G. I. 1922 Tidal oscillations in gulfs and rectangular basins. *Proc. Lond. Math. Soc.* Ser. 2, **20**, 148–181.

TRÖSCH, J. 1984 Finite element calculation of topographic waves in lakes. *Proc. 4th Intl Conf. on Applied Numerical Modeling, Tainan, Taiwan.*